

Forward Modelling of Standing Kink Modes in Coronal Loops I. Synthetic Views

Ding Yuan^{1,2,3}
DYuan2@uc1an.ac.uk

Tom Van Doorsselaere¹

ABSTRACT

Kink magnetohydrodynamic (MHD) waves are frequently observed in various magnetic structures of the solar atmosphere. They may contribute significantly to coronal heating and could be used as a tool to diagnose the solar plasma. In this study, we synthesise the Fe IX $\lambda 171.073$ Å emission of a coronal loop supporting a standing kink MHD mode. The kink MHD wave solution of a plasma cylinder is mapped into a semi-torus structure to simulate a curved coronal loop. We decompose the solution into a quasi-rigid kink motion and a quadrupole term, which dominate the plasma inside and outside the flux tube, respectively. At the loop edges, the line-of-sight integrates relatively more ambient plasma, and the background emission becomes significant. The plasma motion associated with the quadrupole term causes spectral line broadening and emission suppression. The periodic intensity suppression will modulate the integrated intensity and the effective loop width, which both exhibit oscillatory variations at half of the kink period. The quadrupole term can be directly observed as a pendular motion at front view.

Subject headings: Sun: atmosphere — Sun: corona — Sun: oscillations — magnetohydrodynamics (MHD) — waves

1. Introduction

In the past decade, significant progress has been achieved in probing the heating and seismological roles of magnetohydrodynamic (MHD) waves in the solar atmosphere (see reviews by Nakariakov & Verwichte 2005; Liu & Ofman 2014; Jess et al. 2015; Arregui 2015). Among the MHD wave modes, the slow magnetoacoustic mode propagates anisotropically in a low β uniform plasma; the wave energy flows predominantly along the magnetic field line, e.g., De Moor-

tel et al. (2002a,b); Wang et al. (2009a,b); Yuan & Nakariakov (2012); Kumar et al. (2013, 2015); Fang et al. (2015). While fast magnetoacoustic mode could propagate to any direction relative to the magnetic field, i.e., either parallel, perpendicular or oblique, therefore, they are commonly waveguided in a variety of magnetic structures through reflections and refractions. They may couple with Alfvén wave and exhibit mixed wave properties in forms of standing transverse oscillations of coronal loops (Aschwanden & Schrijver 2011; Nisticò et al. 2013; Verwichte et al. 2013a); large-scale coronal propagating fronts across the whole solar disk (Ofman & Thompson 2002; Liu et al. 2010; Guo et al. 2015); quasi-periodic fast wave trains along magnetic funnels (Liu et al. 2012; Yuan et al. 2013; Pascoe et al. 2013; Nisticò et al. 2014b); fast wave pulses across randomly structured plasma (Yuan et al. 2015a); ubiqui-

¹Centre for mathematical Plasma Astrophysics, Department of Mathematics, KU Leuven, Celestijnenlaan 200B bus 2400, B-3001 Leuven, Belgium

²Jeremiah Horrocks Institute, University of Central Lancashire, Preston PR1 2HE, UK

³Key Laboratory of Solar Activity, National Astronomical Observatories, Chinese Academy of Sciences, Beijing, 100012, China

tous propagating kink waves in the entire corona (Tomczyk et al. 2007) and coronal holes (Thurgood et al. 2014; Morton et al. 2015).

Kink waves (the $m = 1$ mode, Edwin & Roberts 1982, 1983; Ruderman 2003; Erdélyi & Morton 2009; Goossens et al. 2014) were initially observed in active region loops in the Extreme Ultraviolet (EUV) channels of the Transition Region and Coronal Explorer (TRACE, Nakariakov et al. 1999; Aschwanden et al. 1999). The coronal loops were observed to oscillate transversely with amplitudes at megametre scale in response to flares, i.e., the associated mass ejections (Schrijver et al. 2002; Zimovets & Nakariakov 2015), filament destabilizations (Schrijver et al. 2002), magnetic reconnection (He et al. 2009), or vortex shedding (Nakariakov et al. 2009). Recently, Nisticò et al. (2013) and Anfinogentov et al. (2013) detected low-amplitude (sub-megametre scale) kink oscillations of coronal loops. Kink waves in this category last for dozens of wave cycles without significant damping, and are apparently not associated with any explosive events (Anfinogentov et al. 2013). Transverse oscillatory motions were also observed in chromospheric spicules (Okamoto & De Pontieu 2011; Morton 2014), chromospheric mottles (Kuridze et al. 2012), filament threads (Lin et al. 2007, 2009), large prominences (Tripathi et al. 2009; Hershaw et al. 2011; Arregui et al. 2012), polar plumes (Thurgood et al. 2014), coronal rain (Antolin & Verwichte 2011), helmet streamers (Chen et al. 2010, 2011), and even coronal mass ejections (Lee et al. 2015).

Fundamental (global) standing kink modes are frequently observed in closed coronal loops (Van Doorselaere et al. 2009; Ruderman & Erdélyi 2009). The period of coronal transverse waves ranges from 2 min to 33 min; and the damping time has a similar time scale (Aschwanden et al. 2002; White & Verwichte 2012). The curved coronal loops are normally assumed to be approximately co-planar; the loop plane intrinsically defines horizontally and vertically polarized kink waves about the loop axis (Ruderman 2009). Horizontal kink waves are more frequently observed, e.g., Nakariakov et al. (1999); Schrijver et al. (2002); Aschwanden et al. (2002); Zimovets & Nakariakov (2015); while vertical kink waves were only reported in a limited number of cases, e.g., Wang & Solanki (2004); Verwichte et al. (2006);

Selwa et al. (2007, 2010, 2011); White et al. (2012); Kim et al. (2014).

The main interest in standing kink modes of coronal loops arises mainly from their role in diagnosing the coronal plasma via MHD seismology (Nakariakov & Verwichte 2005; De Moortel & Nakariakov 2012). The standing kink mode could be used as a tool to infer magnetic field strength along a coronal loop (Nakariakov & Ofman 2001; Verwichte et al. 2009, 2010, 2013a). Verwichte et al. (2013b) measured the range of the density contrast and inhomogeneity layer thickness of coronal loops based on the period-damping time scaling law. De Moortel & Pascoe (2009) are the first to validate MHD seismology with three-dimensional numerical simulations, and showed that the inverted magnetic field strength agrees with the input magnetic field within a factor of about two. Aschwanden & Schrijver (2011) and Verwichte et al. (2013a) compared the seismological field and the Alfvén-transit-time-averaged value in the potential field model, and found consistency within an order of magnitude. Chen & Peter (2015) performed MHD simulations using a realistic coronal model, and found that the excited coronal loop oscillations would be effectively used to infer the average magnetic field.

Kink MHD waves are highly-incompressible in the long wavelength limit and exhibit only quasi-rigid motions (Goossens et al. 2012). Indeed, in a coronal loop the density (or temperature) perturbation by a kink mode is at the order of 10^{-3} or less of the equilibrium value. The observed intensity variations of coronal loops (e.g., O'Shea et al. 2007; Verwichte et al. 2009, 2010) are ascribed to the column depth modulation introduced by the kink motion. Cooper et al. (2003a,b) performed line-of-sight (LOS) integration through the coronal loop plasma perturbed by MHD waves and demonstrated that intensity modulation could become significant in case of a kink mode, even though the plasma fluid compression is negligible.

Recently, Goossens et al. (2014) showed that the kink mode solution could be decomposed into a quasi-rigid transverse motion and a rotational motion, which is detectable as Doppler velocity oscillations in optically thick lines. It confronts interpreting rotational motion as a signature of Alfvén wave (De Pontieu et al. 2012). Therefore, forward modelling would significantly advance the

knowledge of kink modes and resolve the dispute on whether a wave with observed rotational motion is a kink or Alfvén wave (e.g., [Van Doorselaere et al. 2008](#)). Moreover, MHD seismology and wave energy estimation strongly rely on correct identification of the wave mode and accurate measurements of wave properties ([Goossens et al. 2012](#); [Van Doorsselaere et al. 2014](#)).

Forward modelling is a novel approach that synthesizes the plasma emission observables ([Antolin & Van Doorsselaere 2013](#); [Yuan et al. 2015b](#)). It basically converts analytical or numerical models into observables. Therefore, the inversion process (e.g., MHD seismology, MHD spectroscopy, helioseismology, x-ray tomography), which is originally ill-posed owing to the lack of sufficient constraints (or observables), could be better understood in the sense that knowledge of plasma properties is given a priori. [Gruszecki et al. \(2012\)](#) studied the geometric integration of the plasma density of a fast sausage mode of a plasma cylinder. [De Moortel & Bradshaw \(2008\)](#) demonstrated that the damping rate measured in EUV emission intensity oscillations may not reflect the real damping of MHD waves. [Antolin & Van Doorsselaere \(2013\)](#) and [Antolin et al. \(2014\)](#) considered the inhomogeneous plasma emission introduced by fast sausage modes and found that the LOS effect and spatial resolution would significantly modify the associated EUV emissions of coronal loops. [Yuan et al. \(2015b\)](#) found that the contribution function of atomic emission ([Dere et al. 1997](#)) could cause emission asymmetry for positive and negative temperature perturbations, and could even lead to the detection of half periodicity.

In this study, we present the forward modelling study of standing kink modes of coronal loops. Section 2 gives the analytical solution of kink mode in a coronal loop and the numerical discretization for the forward modelling code¹. Section 3 and Section 4 present the results and conclusion, respectively.

¹The FoMo code is available at <https://github.com/TomVeeDee/FoMo>

2. Model

2.1. Standing kink mode

In this paper, we study the standing kink wave in a plasma cylinder embedded in a uniform plasma. The magnetic field is parallel to the axis of the plasma cylinder (i.e., z -axis), $\mathbf{B}_0 = B_0 \hat{\mathbf{z}}$. The equilibrium magnetic field B_0 , plasma density ρ_0 and temperature T_0 are piecewise functions of the r -coordinate:

$$B_0, \rho_0, T_0 = \begin{cases} B_i, \rho_i, T_i, & \text{for } r \leq a \\ B_e, \rho_e, T_e, & \text{for } r > a, \end{cases} \quad (1)$$

where a is the radius of the loop. Hereafter, we use subscript ‘i’ and ‘e’ to differentiate the internal and external equilibrium values of the loop system.

The linearised ideal MHD equations give the perturbed quantities that deviate from the magnetostatic equilibrium (see, e.g., [Ruderman & Erdélyi 2009](#)):

$$\rho_1 = -\nabla \cdot (\rho_0 \boldsymbol{\xi}), \quad (2)$$

$$\rho_0 \frac{\partial^2 \boldsymbol{\xi}}{\partial t^2} = -\nabla P_{T1} + \frac{1}{\mu_0} [(\mathbf{B}_0 \cdot \nabla) \mathbf{b}_1 + (\mathbf{b}_1 \cdot \nabla) \mathbf{B}_0], \quad (3)$$

$$\mathbf{b}_1 = \nabla \times (\boldsymbol{\xi} \times \mathbf{B}_0), \quad (4)$$

$$p_1 - C_s^2 \rho_1 = \boldsymbol{\xi} \cdot (C_s^2 \nabla \rho_0 - \nabla p_0), \quad (5)$$

where $\boldsymbol{\xi}$ is the Lagrangian displacement vector, ρ_0 , p_0 and \mathbf{B}_0 are the plasma density, pressure and magnetic field in equilibrium, ρ_1 , p_1 and \mathbf{b}_1 are the perturbed plasma density, pressure and magnetic field, $P_{T1} = p_1 + \mathbf{b}_1 \cdot \mathbf{B}_0 / \mu_0$ is the perturbed total pressure, μ_0 is the magnetic permeability in free space. A few typical speeds are defined to describe the loop system: $C_s = \sqrt{\gamma p_0 / \rho_0}$, $C_A = B_0 / \sqrt{\mu_0 \rho_0}$, $C_T = C_A C_s / \sqrt{C_A^2 + C_s^2}$ are the acoustic, Alfvén, and tube speed, respectively ([Edwin & Roberts 1983](#)); and $\omega_s = C_s k$, $\omega_A = C_A k$, $\omega_T = C_T k$ are the corresponding acoustic, Alfvén, and tube frequencies, where $k = \pi n / L_0$ is the longitudinal wavenumber, n is the longitudinal mode number ($n = 1$ corresponds to the fundamental mode), L_0 is the length of the loop, $\gamma = 5/3$ is the adiabatic index.

The boundary value problem (Equation 2-5) is solved in cylindrical coordinates (r, ϕ, z) with the Neumann boundary conditions at $r = a$,

$$[P_T]_{r=a} = 0, \quad (6)$$

$$[\xi_r]_{r=a} = 0, \quad (7)$$

and the Dirichlet boundary conditions at $r = 0, \infty$

$$P_T|_{r=0} < \infty, \quad (8)$$

$$\xi^2|_{r=0} < \infty, \quad (9)$$

$$P_T|_{r \rightarrow \infty} = 0, \quad (10)$$

$$\xi^2|_{r \rightarrow \infty} = 0, \quad (11)$$

where P_T and ξ_r are the total pressure and the radial displacement, respectively. In the case of the standing kink mode ($m = 1$), we Fourier-analyse the perturbed quantities by assuming $P_{T1} = A\mathcal{R}(r) \cos(\omega t) \sin(kz) \cos(\phi)$, where A is the amplitude of the perturbed total pressure. The longitudinal profile $\sin(kz)$ ensures that the transverse displacement follows a $\sin kz$ -distribution, and therefore has a maximum at the loop apex for the fundamental mode ($n = 1$).

The perturbed total pressure P_{T1} (and \mathcal{R}) must satisfy

$$\frac{d^2 P_{T1}}{dr^2} + \frac{dP_{T1}}{rdr} - (\kappa_r^2 + \frac{1}{r^2})P_{T1} = 0, \quad (12)$$

where $\kappa_r^2 = \frac{(\omega_s^2 - \omega^2)(\omega_A^2 - \omega^2)}{(\omega_s^2 + \omega_A^2)(\omega_T^2 - \omega^2)}k^2$ is the square of the radial wavenumber and has the dimensionality of wavenumber k^2 . Equation 12 holds for both internal and external plasma, where all quantities are piecewise functions of r , and gives $\mathcal{R} = J_1(|\kappa_{ri}|r)$ or $K_1(\kappa_{re}r)$ for $r < a$ and $r > a$, respectively, where J_1 and K_1 are the first order Bessel function of the first kind and the first order modified Bessel function of the second kind, respectively. We re-define $|\kappa_{ri}| = \sqrt{-\kappa_{ri}^2}$, so the dispersion relation for the fast body mode is obtained:

$$\frac{\kappa_{re}}{\rho_e(\omega_{Ae}^2 - \omega^2)} \frac{K_1'(\kappa_{re}a)}{K_1(\kappa_{re}a)} = \frac{|\kappa_{ri}|}{\rho_i(\omega_{Ai}^2 - \omega^2)} \frac{J_1'(|\kappa_{ri}|a)}{J_1(|\kappa_{ri}|a)}. \quad (13)$$

The perturbed Lagrangian quantities used in the Forward Modelling code are:

$$v_r = \hat{v}_r(r) \sin(\omega t) \sin(kz) \cos \phi, \quad (14)$$

$$v_\phi = \hat{v}_\phi(r) \sin(\omega t) \sin(kz) \sin \phi, \quad (15)$$

$$v_z = \hat{v}_z(r) \sin(\omega t) \cos(kz) \cos \phi, \quad (16)$$

$$\rho_1 = \hat{\rho}_1(r) \cos(\omega t) \sin(kz) \cos \phi, \quad (17)$$

$$T_1 = \hat{T}_1(r) \cos(\omega t) \sin(kz) \cos \phi, \quad (18)$$

where

$$\hat{v}_r = -\frac{r d\mathcal{R}}{\mathcal{R} dr} \hat{v}_0(r), \quad (19)$$

$$\hat{v}_\phi = \hat{v}_0(r) = \frac{A\mathcal{R}\omega}{r\rho_0(\omega^2 - \omega_A^2)}, \quad (20)$$

$$\hat{v}_z = -\frac{C_T^2 k r (\omega^2 - \omega_A^2)}{C_A^2 (\omega^2 - \omega_T^2)} \hat{v}_0, \quad (21)$$

$$\hat{\rho}_1 = \frac{(\omega^2 - \omega_A^2)}{(\omega^2 - \omega_T^2)} \frac{\rho_0 r \omega \hat{v}_0}{(C_s^2 + C_A^2)}, \quad (22)$$

$$\hat{T}_1 = \frac{(\omega^2 - \omega_A^2)}{(\omega^2 - \omega_T^2)} \frac{(\gamma - 1) T_0 r \omega \hat{v}_0}{(C_s^2 + C_A^2)}. \quad (23)$$

The horizontally polarised kink mode has

$$v_x = \tilde{v}_x(r, \phi) \sin(\omega t) \sin(kz), \quad (24)$$

$$v_y = \tilde{v}_y(r, \phi) \sin(\omega t) \sin(kz), \quad (25)$$

where

$$\tilde{v}_x = \hat{v}_r \cos^2 \phi - \hat{v}_\phi \sin^2 \phi \quad (26)$$

$$= \begin{cases} v_{00}(J_0 - J_2 \cos 2\phi), & \text{for } r \leq a \\ -\frac{J_1'(|\kappa_{ri}|a)}{K_1'(\kappa_{re}a)} v_{00}(K_0 + K_2 \cos 2\phi), & \text{for } r > a, \end{cases} \quad (27)$$

$$\tilde{v}_y = \hat{v}_r \cos \phi \sin \phi + \hat{v}_\phi \cos \phi \sin \phi \quad (28)$$

$$= \begin{cases} -v_{00} J_2 \sin 2\phi, & \text{for } r \leq a \\ -\frac{J_1'(|\kappa_{ri}|a)}{K_1'(\kappa_{re}a)} v_{00} K_2 \sin 2\phi, & \text{for } r > a, \end{cases} \quad (29)$$

and $v_{00} = -\frac{A_i \omega |\kappa_{ri}|}{2\rho_i(\omega^2 - \omega_{Ai}^2)}$ is the Lagrangian velocity at the $r = 0$.

We could see that the plasma motion is predominantly polarised along the x-direction described by the J_0 term (also see Appendix A and Goossens et al. 2014). The quadrupole terms $J_2 \cos(2\phi)$ and $J_2 \sin(2\phi)$ may contribute to the fine structuring of coronal loops associated with kink modes. The vertically polarised transverse mode could be easily obtained by replacing ϕ with $\phi + \pi/2$, while keeping the coordinate system intact.

We rewrite Equations 27 and 29 as

$$\begin{bmatrix} \tilde{v}_x \\ \tilde{v}_y \end{bmatrix} = \begin{bmatrix} \tilde{v}_x^{[1]} \\ \tilde{v}_y^{[1]} \end{bmatrix} + \begin{bmatrix} \tilde{v}_x^{[2]} \\ \tilde{v}_y^{[2]} \end{bmatrix}, \quad (30)$$

$$\begin{bmatrix} \tilde{v}_x^{[1]} \\ \tilde{v}_y^{[1]} \end{bmatrix} = \begin{cases} v_{00} \begin{bmatrix} J_0 \\ 0 \end{bmatrix}, & \text{for } r \leq a, \\ -\frac{J'_1(|\kappa_{ri}|a)}{K'_1(\kappa_{re}a)} v_{00} \begin{bmatrix} K_0 \\ 0 \end{bmatrix}, & \text{for } r > a, \end{cases} \quad (31)$$

$$\begin{bmatrix} \tilde{v}_x^{[2]} \\ \tilde{v}_y^{[2]} \end{bmatrix} = \begin{cases} -v_{00} J_2 \begin{bmatrix} \cos 2\phi \\ \sin 2\phi \end{bmatrix}, & \text{for } r \leq a \\ -\frac{J'_1(|\kappa_{ri}|a)}{K'_1(\kappa_{re}a)} v_{00} K_2 \begin{bmatrix} \cos 2\phi \\ \sin 2\phi \end{bmatrix}, & \text{for } r > a. \end{cases} \quad (32)$$

In the thin flux tube limit ($ka \ll 1$), $J_0 = 1 + \mathcal{O}((ka)^2)$ for $r < a$, and $K_0/K_2 \ll 1$ for $r > a$, so the polarized quasi-rigid motion is almost confined within the tube $r < a$ (Figure 1b). The quadrupole term is of secondary effect, as $J_2 = \mathcal{O}((ka)^2)$ for $r < a$, whereas at $r > a$, $K_2/K_0 \gg 1$, so it dominates the surrounding plasma (Figure 1c). But we shall note that the quadrupole term is only a second order term inside the tube, whereas at the ambient plasma, its magnitude is of the first order.

2.1.1. Correction for advected plasma motion

Equations 14-18 are solutions in Lagrangian coordinates, while we need to synthesize observables at a fixed LOS (Eulerian coordinates), therefore, the Lagrangian variables are remapped into Eulerian coordinates. The transverse displacement of a kink mode is of the order of the loop radius a (Aschwanden et al. 2002), and therefore, the advected motion cannot be neglected. The displacement ξ for the plasma fluid at initial position $[r, \phi, z]$ could be obtained by integrating the velocity with respect to time t .

$$\xi_r = -\hat{v}_r/\omega \cos(\omega t) \sin(kz) \cos \phi, \quad (33)$$

$$\xi_\phi = -\hat{v}_\phi/\omega \cos(\omega t) \sin(kz) \sin \phi, \quad (34)$$

$$\xi_z = -\hat{v}_z/\omega \cos(\omega t) \cos(kz) \cos \phi. \quad (35)$$

In Cartesian coordinates, the displacement is given as,

$$\xi_x = \tilde{\xi}_x \cos(\omega t) \sin(kz), \quad (36)$$

$$\xi_y = \tilde{\xi}_y \cos(\omega t) \sin(kz), \quad (37)$$

where $[\tilde{\xi}_x, \tilde{\xi}_y]^T = -[\tilde{v}_x, \tilde{v}_y]^T/\omega$. Then the new position $[\tilde{x}, \tilde{y}, \tilde{z}]^T$ of the plasma fluid originally at $[x, y, z]^T = [r \cos \phi, r \sin \phi, z]^T$ is

$$\tilde{x}(t) = x + \xi_x(t), \quad (38)$$

$$\tilde{y}(t) = y + \xi_y(t), \quad (39)$$

$$\tilde{z}(t) = z + \xi_z(t). \quad (40)$$

Thus, the plasma properties (e.g. $\rho_0 + \rho_1$) at location $[x, y, z]^T$ will be moved to the position $[\tilde{x}, \tilde{y}, \tilde{z}]^T$.

2.1.2. Mapping into a semi-torus structure

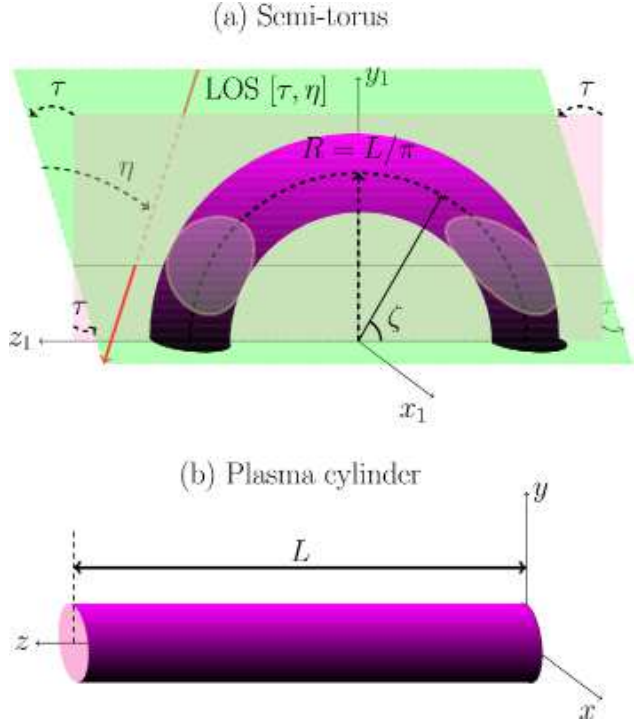


Fig. 2.— Schematic drawing illustrates how the cylinder is mapped into a semi-torus and the LOS angle definition. The pink plane ($y_1 z_1$ plane) is defined by the loop spine. The green plane forms an angle of τ with the pink plane; and their line of intersection is parallel with the z_1 -axis. The LOS is free to vary within the green plane and quantified by an angle $\eta + \pi/2$ relative to the z_1 -axis or the line of intersection. A LOS angle is denoted as $[\tau, \eta]$.

The loop curvature was found to have a secondary effect on the transverse motion of coronal

loops (Van Doorselaere et al. 2009), and therefore we only consider the LOS effect and plasma inhomogeneities by mapping the kink mode solution of a plasma cylinder into a semi-torus structure (see Figure 2). The kink mode displaces the axis of the loop, therefore, it has a polarisation relative to the plane defined by the static curved loop axis, i.e., the y_1z_1 plane. It is defined as a horizontal kink mode if the loop oscillates out of the y_1z_1 plane (e.g., Nakariakov et al. 1999; Aschwanden et al. 1999). Or otherwise, if the transverse motion of the loop axis is within the y_1z_1 plane, it is termed as a vertical kink mode (e.g., Wang & Solanki 2004; Verwichte et al. 2006).

After correcting the advected motion, we map the plasma coordinates and the associated plasma parameters into a semi-torus structure (Figure 2). The plasma cylinder is bent into a torus within the y_1z_1 plane, using the following transform (also see Kuznetsov et al. 2015):

$$x_1 = x, \quad (41)$$

$$y_1 = (R + y) \sin \zeta, \quad (42)$$

$$z_1 = -(R + y) \cos \zeta, \quad (43)$$

where $\zeta = z/R$, and $R = L/\pi$.

The velocity is transformed by

$$\begin{bmatrix} v_{x_1} \\ v_{y_1} \\ v_{z_1} \end{bmatrix} = \begin{bmatrix} 1 & 0 & 0 \\ 0 & \sin \zeta(z) & \cos \zeta(z) \\ 0 & -\cos \zeta(z) & \sin \zeta(z) \end{bmatrix} \begin{bmatrix} v_x \\ v_y \\ v_z \end{bmatrix}. \quad (44)$$

This is basically a rotation of the velocity vector by an angle of $\zeta - \pi/2$ about the x -axis; and $\zeta - \pi/2$ varies within $[-\pi/2, \pi/2]$ for $z \in [0, L]$.

2.2. Coronal loop model

Coronal loops are highly complex and dynamic structures, observed within a broad range of plasma conditions, see a review by Reale (2014). The loop width varies from a few hundreds (Brooks et al. 2013; Morton & McLaughlin 2013) to dozens of thousands kilometres (Aschwanden et al. 2002; Aschwanden & Nightingale 2005; Aschwanden & Schrijver 2011). A coronal loop may have multi-thermal (Nisticò et al. 2014a), multi-stranded structures (Scullion et al. 2014; Peter et al. 2013), and may be associated with heating and flows (Klimchuk 2006; Hood et al. 2009; Winebarger et al. 2002). In our study, these fine

structures are not considered; and the gravitational stratification is also neglected. Numerical simulations are required to model these features of coronal loop oscillations.

A coronal loop is set up in an equilibrium state. The loop measures $L_0 = 100$ Mm in length and $a = 4$ Mm in radius. The loop density and temperature are $\rho_i = 2.5 \cdot 10^{-12} \text{ kg} \cdot \text{m}^{-3}$ ($n_{ei} = 1.5 \cdot 10^9 \text{ cm}^{-3}$) and $T_i = 0.8$ MK, respectively. The internal plasma is permeated by a uniform magnetic field $B_i = 15$ G. We choose a density and temperature ratio of $\rho_i/\rho_e = 5$ and $T_i/T_e = 1.5$, respectively, then the magnetic field strength ratio is obtained by balancing the total pressure at the loop boundary. The plasma beta gives $\beta_i = 0.037$ and $\beta_e = 0.0048$ for the internal and external plasma, respectively. The corresponding acoustic speeds are $C_{si} = 150 \text{ km s}^{-1}$ and $C_{se} = 120 \text{ km s}^{-1}$, while the Alfvén speeds are $C_{Ai} = 840 \text{ km s}^{-1}$ and $C_{Ae} = 1900 \text{ km s}^{-1}$. These parameters are commonly observed in coronal loops (e.g., Reale 2014; Aschwanden & Boerner 2011).

For the fundamental mode ($n = 1$), the wavelength is much longer than the loop radius ($ka = 0.13$). The dispersion relationship (Equation 13) finds a kink mode solution with a period at $P_0 = 3.0$ min ($\omega = 0.034$). We choose $A_i = 0.15$ Pa, so that the velocity perturbation amplitude is about 55 km s^{-1} , and the amplitude of displacement about 1.6 Mm ($0.4a$). The kink mode could be considered as highly incompressible (Van Doorselaere et al. 2008; Goossens et al. 2012), the density (temperature) perturbation is about 0.4% (0.3%) of the equilibrium value. These parameters are commonly observed by the TRACE and SDO/AIA instruments (Aschwanden et al. 2002; Aschwanden & Schrijver 2011).

2.3. Forward model

The loop system was discretised as given by Equations 14-18 in Cartesian coordinates. We calculate the plasma properties in a domain of $x(y) \in [-2a, 2a]$ and $z \in [0, L_0]$ with $160 \times 160 \times 400$ grid cells. Forward modelling was performed with a fixed output mesh grid $N_{x_2} \times N_{y_2} = 170 \times 340$ ² (see details in Yuan et al. 2015b). In contrast to compressive MHD modes (Antolin & Van Doorselaere 2013; Reznikova et al. 2014, 2015; Kuznetsov

²We refer to the projected output plane as x_2y_2 plane.

et al. 2015; Yuan et al. 2015b), the kink mode only perturbs the density and temperature to the order of 10^{-3} - 10^{-4} of the equilibrium values, therefore the effect of the contribution function is of secondary order. The spatial distributions of the plasma properties play a key role in determining the observational features. So we only present the synthetic emission of the Fe IX $\lambda 171.073$ Å line, however, the results should be applicable to other optically thin lines. The Fe XII $\lambda 193.509$ Å line and the AIA 171 and 193 Å channel were also synthesised, but they only produce redundant results.

The LOS is defined with two independent angles $[\tau, \eta]$ (see illustration in Figure 2), where τ is the angle between the loop axis plane (pink plane or y_1z_1 -plane) and another plane (green plane), which share a line of intersection parallel to the z_1 -axis. The LOS forms an angle of $\eta + \pi/2$ relative to the z_1 -axis (or the line of intersection). Hereafter, we name $[0^\circ, 0^\circ]$ as top view, $[0^\circ, 90^\circ]$ as side view, $[90^\circ, 0^\circ]$ as front view, and $[45^\circ, 0^\circ]$ as oblique view for reference. Figure 3 illustrates the synthetic views in the Fe IX $\lambda 171.073$ Å line at selected viewing angles; while Figure 4 presents the spectra of the Fe IX $\lambda 171.073$ Å line along a slice s perpendicular to the axis of the loop apex at each viewing angle, which is comparable with Figure 9 in Goossens et al. (2014). We note that the loop cross-sectional profile could be approximated by integrating the emissivity along a uniform media $2\sqrt{a^2 - r^2}$, thus gives a non-Gaussian profile. However, a Gaussian profile is normally assumed and practically observed, e.g., Verwichte et al. (2005); Aschwanden & Boerner (2011). It implies that coronal loops could be multi-thermal (e.g., Nisticò et al. 2014a), multi-stranded (Peter et al. 2013) or inhomogeneous (Van Doorsselaere et al. 2004). However, the point spread function may also play a role, especially in low resolution instruments. Inhomogeneity in a coronal loop is favoured by the resonant absorption theory (Ruderman & Roberts 2002; Van Doorsselaere et al. 2004; Okamoto et al. 2015; Antolin et al. 2015), which is developed to explain the strong damping of kink waves (Nakariakov et al. 1999). In this study, we do not consider the resonant absorption layer.

3. Results

3.1. Top view

Figure 5 presents snapshots of the relative emission intensity I/I_m , Doppler shift velocity v_D and line width w at top view, where I_m is the maximum intensity of the synthetic image series in each viewing angle. At top view, the loop oscillates within the plane-of-sky, it is clearly seen in the relative intensity, Doppler shift velocity, and line width snapshots. The loop motion is not effectively observed in the Doppler shift, as the plasma motion inside and outside the loop is perpendicular to the LOS.

Figure 6 shows the sit-and-stare mode of a spectrograph, e.g., Hinode/EIS, in the Fe IX $\lambda 171.073$ Å line. The time distance plot (see, e.g., Yuan & Nakariakov 2012) is taken at a cut perpendicular to the loop axis, see Figure 5. It clearly shows the transverse loop motion with an amplitude of about 1.5 Mm ($0.4a$); the associated intensity modulation is about 0.04. Intriguingly, we also detect loop width (Full-Width at Half-Maximum) variation between 7.0 Mm ($1.7a$) to 7.4 Mm ($1.8a$); the amplitude is about 0.2 Mm, one order of magnitude smaller than the loop displacement. The periodicity of the loop width and intensity variation is $P_0/2$. The Doppler shift velocity v_D is close to zero both inside and outside the loop. Moreover, one could also observe line broadening on the loop periphery. The Doppler shift has the same periodicity P_0 , but $\pi/4$ out of phase with the transverse motion. The line width variation has a period of $P_0/2$, and oscillates with a phase of $\pi/2$ lagging behind the loop intensity variation. Figure 4 (right column) illustrates this effect: the spectrum moves as a whole in space due to the transverse motion, however, the centroid of the spectrum remains unchanged, i.e., $v_D \simeq 0$ km s. At the loop periphery, one could observe significant periodic broadening. The background emission, about 2% of the loop emission, is associated with the quadrupole terms in Equations 27 and 29 (see Appendix A for derivations).

3.2. Front view

At front view, the transverse motion is along the LOS, so the measured loop displacement is almost zero (Figure 7). The Doppler shift veloc-

ity and line width broadening at the loop edges are detectable. The time-distance plot (Figure 8) shows that the loop width oscillates with an amplitude of $0.1a$ and a period of $P_0/2$. The amplitude (about $0.1a$) observed at front view is about twice that (about $0.05a$) measured at top view. Again, we detect line width broadening at the periphery of the loop. This effect may contribute to the non-thermal broadening that has been observed at the edge of active region loops (Doscchek et al. 2007). The associated Doppler shift (about 5 km s^{-1}) of the ambient plasma still exists (Figure 8), however, in contrast to the apparent rotational motion at top view, the oscillation resembles a pendular motion relative to the loop oscillation. Figure 4 (left column) illustrates this effect: the Doppler shift on the periphery of the loop oscillates in anti-phase with the kink motion inside the loop, but with an amplitude of about 10% of the loop oscillation. This is consistent with Figure 9 in Goossens et al. (2014).

3.3. Oblique view

Oblique view (Figure 9) is the most frequently encountered observation on the solar disk. Figure 10 shows the time-distance plot observed in the Fe IX $\lambda 171.073 \text{ \AA}$ line. Loop oscillation features at oblique view contain a mixture of the properties observed at top and front views: loop displacement, intensity modulation and loop width vary at moderate levels.

3.4. Side view

Side view and its varieties are the most probable viewing angles for off-limb coronal loops, see, e.g., Verwichte et al. (2004). Figure 11 displays a complete cycle of the standing kink wave at side view. Loop displacement is optimal for observation in the intensity; while the Doppler shift is very small. The line width does not exhibit significant spatial variation over the projected loop. However, line broadening is significantly measurable. The maximum line width broadening is not located at the loop apex, this is because at the apex the plasma motion is almost perpendicular, rather than along the LOS, and the projected fluid motion is only significant at some distance away from the apex.

Figure 12 presents the time-distance plot at the

loop apex and the time series of the loop position, width and intensity variations. The times series of the transverse motion is close to a sinusoidal profile, while in other viewing angles the loop displacement deviates significantly from a harmonic function. We note that at side view, the loop width measures at $\simeq 8 \text{ Mm}$ (about $2a$), whereas other viewing angles normally do not reveal the full width of the loop. The associated loop width and intensity variations are very small.

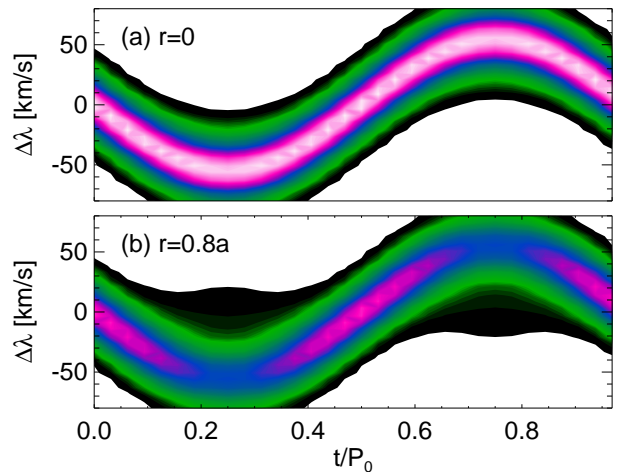


Fig. 13.— Dynamic spectra extracted at positions $r = 0$ (a) and $r = 0.8a$ (b) at front view, as labeled in Figure 7.

4. Discussion and Conclusion

In this study, we discretised the fundamental standing kink wave solution of a plasma cylinder, corrected for the fluid advection, and mapped the solution into a semi-torus structure to simulate the kink MHD mode of a curved coronal loop. Then, we synthesised the EUV emission in the Fe IX $\lambda 171.073 \text{ \AA}$ line and performed Gaussian fits to the spectra to obtain the observables, i.e., the emission intensity, Doppler shift velocity and line width.

We find that the cross-sectional intensity distribution of a coronal loop filled with uniform plasma does not follow a Gaussian profile. It means complex coronal loop structure has to be considered to fully synthesize loop oscillations. More physics is associated with loop inhomogeneities, i.e., resonant absorption (Ruderman & Roberts 2002; Van

Doorsselaere et al. 2004), phase mixing (Heyvaerts & Priest 1983), mode conversion (Pascoe et al. 2010, 2011, 2012).

Loop displacement could be observed in any viewing angles, as long as the polarised motion is not along the LOS. This is the intrinsic feature of a kink MHD wave.

Since the density and temperature perturbations are of the order of 10^{-3} - 10^{-4} of the equilibrium values, the contribution function has a negligible effect on the loop intensity modulation. The kink mode solution could be decomposed into a quasi-rigid transverse motion and a quadrupole term. The quadrupole term appears in both the v_x and v_y components of the transverse velocity (Equations 27 and 29). **The fluid elements at $[r, \phi]$ and $[r, -\phi]$ (or equally $[r, \phi]$ and $[r, \pi - \phi]$) outside the tube would periodically deform the r -shell in the Lagrangian coordinate at the order of $2 \frac{J'_1(|\kappa_{ri}|a)}{K'_1(\kappa_{re}a)} v_{00} K_2/\omega$ (see Equations 31 and 32), which is a few percent of the loop radius a , if the amplitude of the displacement is close to a . Moreover, the fluid elements at $\pm\phi$ of the r -shell move to the opposite directions (Figure 14), and thus cause spectral line broadening. The broadening is also accompanied by intensity suppression as illustrated in Figure 13. At front view, the emission suppression at $r = 0.8a$ is stronger than that at the loop axis. The quadrupole term effect only becomes significant at loop edges, where the LOS integrates through more ambient plasma, and has smaller impact on the spectrum at the loop axis as the major contribution are from the plasma inside the tube.**

Line width broadening is usually measured in the periphery of the loop, where ambient plasma emission is significant. It is associated with the $\cos(2\theta)$ and $\sin(2\theta)$ terms in Equation 27 and 29. The line broadening is observed at all views. Figure 14 illustrates the reason: at front view v_x could vary from positive to negative along a LOS at loop edge; whereas at top view, v_y is anti-symmetric about the xz -plane. This is consistent with the case of a vertical transverse wave (Van Doorsselaere & Nakariakov 2008). Doschek et al. (2007) reported non-thermal broadening at the edge of active region loops, and it may be connected with kink mode perturbations in the loops. However,

since there is no report of the associated transverse motion, it may imply that coronal loops have unresolved low-amplitude motion similar to Nisticò et al. (2013) and Anfinogentov et al. (2013).

The intensity modulation at the loop axis is usually detectable. This is different with Cooper et al. (2003a,b), which only consider static plasma emission. In our study, both the spectrum modification by the MHD wave motion are considered and measured as what would occur in realistic observations. This factor could contribute to the integrated LOS intensity variation at the loop axis.

At front view and its varieties, a pendular motion is observed. At front view, the transverse motion of the loop could be fully observed along the LOS, while the background emission oscillates at an amplitude of a few percent of the loop oscillation amplitude.

It is intriguing that **coronal loop is observed to have an apparent periodic expansion and contraction** when undergoing a kink MHD mode wave. The optimal viewing angle to observe this effect is the front view. The amplitude of the loop width variation is about 20-30% of the transverse loop motion. At top view, the loop width variation is about half of the amplitude measured at front view. At side view, this effect could not be observed. The loop deformation introduced by the quadrupole terms alone is not fully responsible for the loop width variation at such amplitude. The line width broadening would result in emission intensity suppression at loop edges, and therefore, the effective width of the loop measured in the emission intensity profile is smaller. In such a scenario, one detects effective loop width modulation associated with the periodic re-distribution of the intensity across the loop. Aschwanden & Schrijver (2011) reported loop cross-sectional variations in a vertically polarised standing kink mode and interpreted it as a signature of coupled kink and sausage mode. In our simulation, we predict that loop width oscillates at a similar amplitude, but with half the period of the kink mode. According to our modelling, Aschwanden & Schrijver (2011) may have observed an overlap of a steady loop and an oscillating loop of similar density and temperature distribution. Therefore, the loop width variation could be accurately measured. The second paper (Yuan & Van Doorsselaere 2016) in this series will present the modelling details of this event.

In our loop system, the plasma emission of the coronal loop is about two orders of magnitude larger than the background. If the background emission becomes comparable to that of the loop, the spectroscopic measurement is still valid to some extent (Yuan et al. 2015b). However, one may opt to use another spectral line that is much more sensitive to the plasma emission of interest.

The resolution of the forward models in each view is better than current instruments, i.e., Hinode/EIS. Therefore, to predict the possible observations with EIS, we degrade the resolution to EIS level ($1''$) by averaging with the neighbouring pixel. The red time series in Figures 6, 8, 10, and 12, represent the possible sit-and-stare observations with EIS. The loop width is generally measured to be smaller with low-resolution instruments; while the other parameters appear to be a smoothed version of those measured with high-resolution instruments, e.g., the SPICE instrument onboard the Solar Orbiter.

In this study, we only consider a specific case of a standing kink wave in a coronal loop and synthesise the Fe IX $\lambda 171.073$ Å emissions. However, it should be generally applicable to other optically thin emission lines, because in the kink MHD mode, the perturbations to the density and temperature are very tiny. Therefore the spatial distribution of the velocity field plays a determining role in the observational signatures.

The research was supported by an Odysseus grant of the FWO Vlaanderen, the IAP P7/08 CHARM (Belspo), the Topping-Up grant CorSeis, the GOA-2015-014 (KU Leuven), and the Open Research Program KLSA201504 of Key Laboratory of Solar Activity of National Astronomical Observatories of China (D.Y.). CHIANTI is a collaborative project involving George Mason University, the University of Michigan (USA) and the University of Cambridge (UK).

REFERENCES

- Anfinogentov, S., Nisticò, G., & Nakariakov, V. M. 2013, *A&A*, 560, A107
- Antolin, P., Okamoto, T. J., De Pontieu, B., et al. 2015, *ApJ*, 809, 72
- Antolin, P., & Van Doorselaere, T. 2013, *A&A*, 555, A74
- Antolin, P., & Verwichte, E. 2011, *ApJ*, 736, 121
- Antolin, P., Yokoyama, T., & Van Doorselaere, T. 2014, *ApJ*, 787, L22
- Arregui, I. 2015, *Philosophical Transactions of the Royal Society of London A: Mathematical, Physical and Engineering Sciences*, 373, doi:10.1098/rsta.2014.0261
- Arregui, I., Oliver, R., & Ballester, J. L. 2012, *Living Reviews in Solar Physics*, 9, 2
- Aschwanden, M. J., & Boerner, P. 2011, *ApJ*, 732, 81
- Aschwanden, M. J., de Pontieu, B., Schrijver, C. J., & Title, A. M. 2002, *Sol. Phys.*, 206, 99
- Aschwanden, M. J., Fletcher, L., Schrijver, C. J., & Alexander, D. 1999, *ApJ*, 520, 880
- Aschwanden, M. J., & Nightingale, R. W. 2005, *ApJ*, 633, 499
- Aschwanden, M. J., & Schrijver, C. J. 2011, *ApJ*, 736, 102
- Brooks, D. H., Warren, H. P., Ugarte-Urra, I., & Winebarger, A. R. 2013, *ApJ*, 772, L19
- Chen, F., & Peter, H. 2015, *A&A*, 581, A137
- Chen, Y., Feng, S. W., Li, B., et al. 2011, *ApJ*, 728, 147
- Chen, Y., Song, H. Q., Li, B., et al. 2010, *ApJ*, 714, 644
- Cooper, F. C., Nakariakov, V. M., & Tsiklauri, D. 2003a, *A&A*, 397, 765
- Cooper, F. C., Nakariakov, V. M., & Williams, D. R. 2003b, *A&A*, 409, 325
- De Moortel, I., & Bradshaw, S. J. 2008, *Sol. Phys.*, 252, 101
- De Moortel, I., Hood, A. W., Ireland, J., & Walsh, R. W. 2002a, *Sol. Phys.*, 209, 89
- De Moortel, I., Ireland, J., Walsh, R. W., & Hood, A. W. 2002b, *Sol. Phys.*, 209, 61

- De Moortel, I., & Nakariakov, V. M. 2012, Royal Society of London Philosophical Transactions Series A, 370, 3193
- De Moortel, I., & Pascoe, D. J. 2009, *ApJ*, 699, L72
- De Pontieu, B., Carlsson, M., Rouppe van der Voort, L. H. M., et al. 2012, *ApJ*, 752, L12
- Dere, K. P., Landi, E., Mason, H. E., Monsignori Fossi, B. C., & Young, P. R. 1997, *A&AS*, 125, 149
- DLMS. 2015, NIST Digital Library of Mathematical Functions, <http://dlmf.nist.gov/>, Release 1.0.9 of 2014-08-29, online companion to [Olver et al. \(2010\)](#)
- Doschek, G. A., Mariska, J. T., Warren, H. P., et al. 2007, *ApJ*, 667, L109
- Edwin, P. M., & Roberts, B. 1982, *Sol. Phys.*, 76, 239
- . 1983, *Sol. Phys.*, 88, 179
- Erdélyi, R., & Morton, R. J. 2009, *A&A*, 494, 295
- Fang, X., Yuan, D., Van Doorselaere, T., Kepens, R., & Xia, C. 2015, *ApJ*, 813, 33
- Goossens, M., Andries, J., Soler, R., et al. 2012, *ApJ*, 753, 111
- Goossens, M., Soler, R., Terradas, J., Van Doorselaere, T., & Verth, G. 2014, *ApJ*, 788, 9
- Gruszecki, M., Nakariakov, V. M., & Van Doorselaere, T. 2012, *A&A*, 543, A12
- Guo, Y., Ding, M. D., & Chen, P. F. 2015, *ApJS*, 219, 36
- He, J., Marsch, E., Tu, C., & Tian, H. 2009, *ApJ*, 705, L217
- Hershaw, J., Foullon, C., Nakariakov, V. M., & Verwichte, E. 2011, *A&A*, 531, A53
- Heyvaerts, J., & Priest, E. R. 1983, *A&A*, 117, 220
- Hood, A. W., Browning, P. K., & van der Linden, R. A. M. 2009, *A&A*, 506, 913
- Jess, D. B., Morton, R. J., Verth, G., et al. 2015, *Space Sci. Rev.*, 190, 103
- Kim, S., Nakariakov, V. M., & Cho, K.-S. 2014, *ApJ*, 797, L22
- Klimchuk, J. A. 2006, *Sol. Phys.*, 234, 41
- Kumar, P., Innes, D. E., & Inhester, B. 2013, *ApJ*, 779, L7
- Kumar, P., Nakariakov, V. M., & Cho, K.-S. 2015, *ApJ*, 804, 4
- Kuridze, D., Morton, R. J., Erdélyi, R., et al. 2012, *ApJ*, 750, 51
- Kuznetsov, A. A., Van Doorselaere, T., & Reznikova, V. E. 2015, *Sol. Phys.*, 290, 1173
- Lee, H., Moon, Y.-J., & Nakariakov, V. M. 2015, *ApJ*, 803, L7
- Lin, Y., Engvold, O., Rouppe van der Voort, L. H. M., & van Noort, M. 2007, *Sol. Phys.*, 246, 65
- Lin, Y., Soler, R., Engvold, O., et al. 2009, *ApJ*, 704, 870
- Liu, W., Nitta, N. V., Schrijver, C. J., Title, A. M., & Tarbell, T. D. 2010, *ApJ*, 723, L53
- Liu, W., & Ofman, L. 2014, *Sol. Phys.*, 289, 3233
- Liu, W., Ofman, L., Nitta, N. V., et al. 2012, *ApJ*, 753, 52
- Morton, R. J. 2014, *A&A*, 566, A90
- Morton, R. J., & McLaughlin, J. A. 2013, *A&A*, 553, L10
- Morton, R. J., Tomczyk, S., & Pinto, R. 2015, *Nature Communications*, 6, 7813
- Nakariakov, V. M., Aschwanden, M. J., & van Doorselaere, T. 2009, *A&A*, 502, 661
- Nakariakov, V. M., & Ofman, L. 2001, *A&A*, 372, L53
- Nakariakov, V. M., Ofman, L., Deluca, E. E., Roberts, B., & Davila, J. M. 1999, *Science*, 285, 862
- Nakariakov, V. M., & Verwichte, E. 2005, *Living Reviews in Solar Physics*, 2, 3

- Nisticò, G., Anfinogentov, S., & Nakariakov, V. M. 2014a, *A&A*, 570, A84
- Nisticò, G., Nakariakov, V. M., & Verwichte, E. 2013, *A&A*, 552, A57
- Nisticò, G., Pascoe, D. J., & Nakariakov, V. M. 2014b, *A&A*, 569, A12
- Ofman, L., & Thompson, B. J. 2002, *ApJ*, 574, 440
- Okamoto, T. J., Antolin, P., De Pontieu, B., et al. 2015, *ApJ*, 809, 71
- Okamoto, T. J., & De Pontieu, B. 2011, *ApJ*, 736, L24
- Olver, F. W. J., Lozier, D. W., Boisvert, R. F., & Clark, C. W., eds. 2010, *NIST Handbook of Mathematical Functions* (New York, NY: Cambridge University Press), print companion to [DLMS \(2015\)](#)
- O’Shea, E., Srivastava, A. K., Doyle, J. G., & Banerjee, D. 2007, *A&A*, 473, L13
- Pascoe, D. J., Hood, A. W., de Moortel, I., & Wright, A. N. 2012, *A&A*, 539, A37
- Pascoe, D. J., Nakariakov, V. M., & Kupriyanova, E. G. 2013, *A&A*, 560, A97
- Pascoe, D. J., Wright, A. N., & De Moortel, I. 2010, *ApJ*, 711, 990
- . 2011, *ApJ*, 731, 73
- Peter, H., Bingert, S., Klimchuk, J. A., et al. 2013, *A&A*, 556, A104
- Reale, F. 2014, *Living Reviews in Solar Physics*, 11, 4
- Reznikova, V. E., Antolin, P., & Van Doorselaere, T. 2014, *ApJ*, 785, 86
- Reznikova, V. E., Van Doorselaere, T., & Kuznetsov, A. A. 2015, *A&A*, 575, A47
- Ruderman, M. S. 2003, *A&A*, 409, 287
- . 2009, *A&A*, 506, 885
- Ruderman, M. S., & Erdélyi, R. 2009, *Space Sci. Rev.*, 149, 199
- Ruderman, M. S., & Roberts, B. 2002, *ApJ*, 577, 475
- Schrijver, C. J., Aschwanden, M. J., & Title, A. M. 2002, *Sol. Phys.*, 206, 69
- Scullion, E., Rouppe van der Voort, L., Wedemeyer, S., & Antolin, P. 2014, *ApJ*, 797, 36
- Selwa, M., Murawski, K., Solanki, S. K., & Ofman, L. 2010, *A&A*, 512, A76
- Selwa, M., Murawski, K., Solanki, S. K., & Wang, T. J. 2007, *A&A*, 462, 1127
- Selwa, M., Solanki, S. K., & Ofman, L. 2011, *ApJ*, 728, 87
- Thurgood, J. O., Morton, R. J., & McLaughlin, J. A. 2014, *ApJ*, 790, L2
- Tomczyk, S., McIntosh, S. W., Keil, S. L., et al. 2007, *Science*, 317, 1192
- Tripathi, D., Isobe, H., & Jain, R. 2009, *Space Sci. Rev.*, 149, 283
- Van Doorselaere, T., Andries, J., Poedts, S., & Goossens, M. 2004, *ApJ*, 606, 1223
- Van Doorselaere, T., Gijsen, S. E., Andries, J., & Verth, G. 2014, *ApJ*, 795, 18
- Van Doorselaere, T., & Nakariakov, V. M. 2008, in *Astronomical Society of the Pacific Conference Series*, Vol. 397, *First Results From Hinode*, ed. S. A. Matthews, J. M. Davis, & L. K. Harra, 58
- Van Doorselaere, T., Nakariakov, V. M., & Verwichte, E. 2008, *ApJ*, 676, L73
- Van Doorselaere, T., Verwichte, E., & Terradas, J. 2009, *Space Sci. Rev.*, 149, 299
- Verwichte, E., Aschwanden, M. J., Van Doorselaere, T., Foullon, C., & Nakariakov, V. M. 2009, *ApJ*, 698, 397
- Verwichte, E., Foullon, C., & Nakariakov, V. M. 2006, *A&A*, 452, 615
- Verwichte, E., Foullon, C., & Van Doorselaere, T. 2010, *ApJ*, 717, 458
- Verwichte, E., Nakariakov, V. M., & Cooper, F. C. 2005, *A&A*, 430, L65

- Verwichte, E., Nakariakov, V. M., Ofman, L., & Deluca, E. E. 2004, *Sol. Phys.*, 223, 77
- Verwichte, E., Van Doorselaere, T., Foullon, C., & White, R. S. 2013a, *ApJ*, 767, 16
- Verwichte, E., Van Doorselaere, T., White, R. S., & Antolin, P. 2013b, *A&A*, 552, A138
- Wang, T. J., Ofman, L., & Davila, J. M. 2009a, *ApJ*, 696, 1448
- Wang, T. J., Ofman, L., Davila, J. M., & Mariska, J. T. 2009b, *A&A*, 503, L25
- Wang, T. J., & Solanki, S. K. 2004, *A&A*, 421, L33
- White, R. S., & Verwichte, E. 2012, *A&A*, 537, A49
- White, R. S., Verwichte, E., & Foullon, C. 2012, *A&A*, 545, A129
- Winebarger, A. R., Warren, H., van Ballegooijen, A., DeLuca, E. E., & Golub, L. 2002, *ApJ*, 567, L89
- Yuan, D., & Nakariakov, V. M. 2012, *A&A*, 543, A9
- Yuan, D., Pascoe, D. J., Nakariakov, V. M., Li, B., & Keppens, R. 2015a, *ApJ*, 799, 221
- Yuan, D., Shen, Y., Liu, Y., et al. 2013, *A&A*, 554, A144
- Yuan, D., & Van Doorselaere, T. 2016, *ArXiv e-prints*, arXiv:1602.07598
- Yuan, D., Van Doorselaere, T., Banerjee, D., & Antolin, P. 2015b, *ApJ*, 807, 98
- Zimovets, I. V., & Nakariakov, V. M. 2015, *A&A*, 577, A4

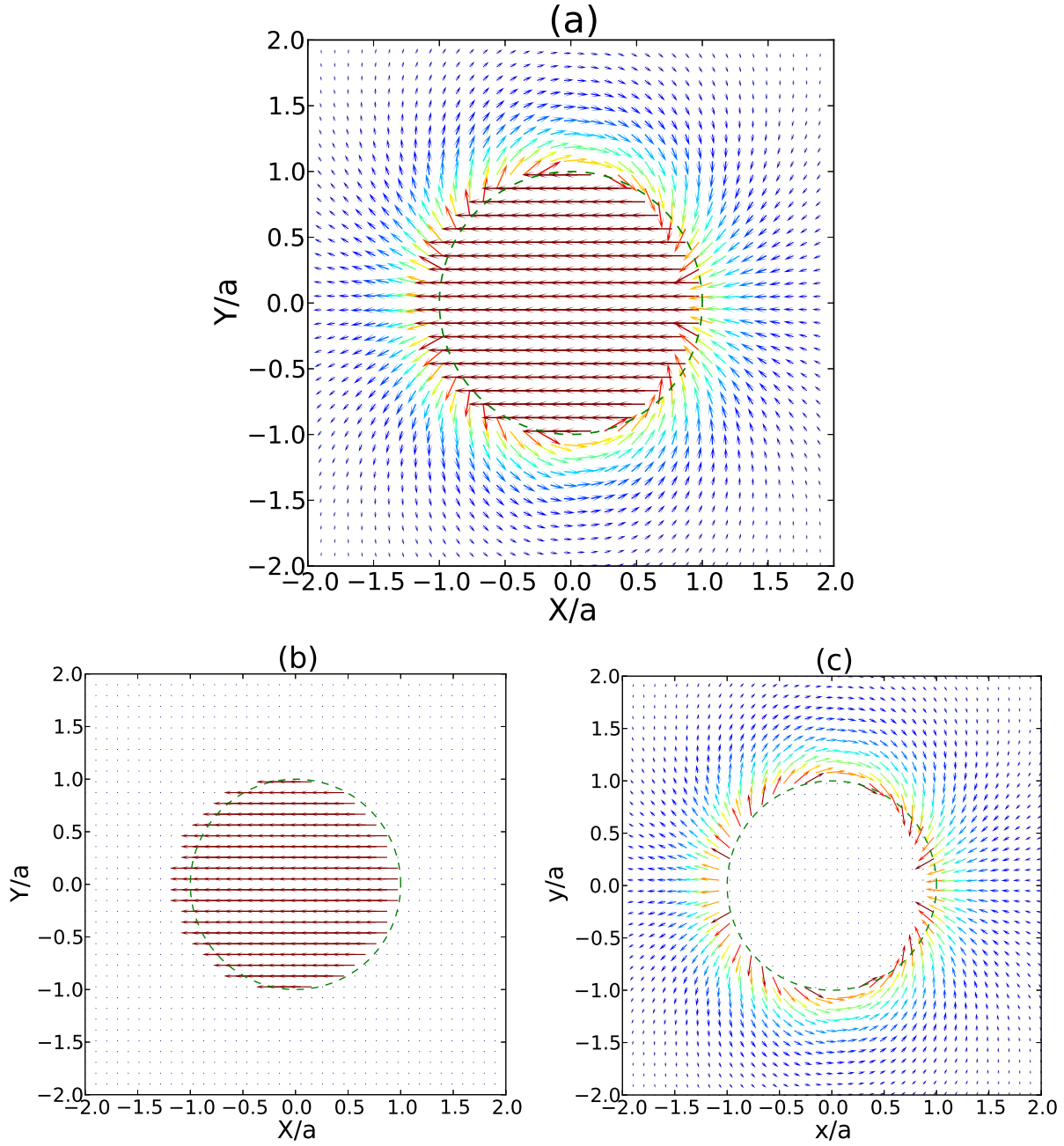


Fig. 1.— Flow fields at cross-section of $z = L_0/2$. (a) illustrates the full solution $[\tilde{v}_x, \tilde{v}_y]^T$, whereas (b) and (c) shows the polarized quasi-rigid motion $[\tilde{v}_x^{[1]}, \tilde{v}_y^{[1]}]^T$ and the quadrupole term $[\tilde{v}_x^{[2]}, \tilde{v}_y^{[2]}]^T$.

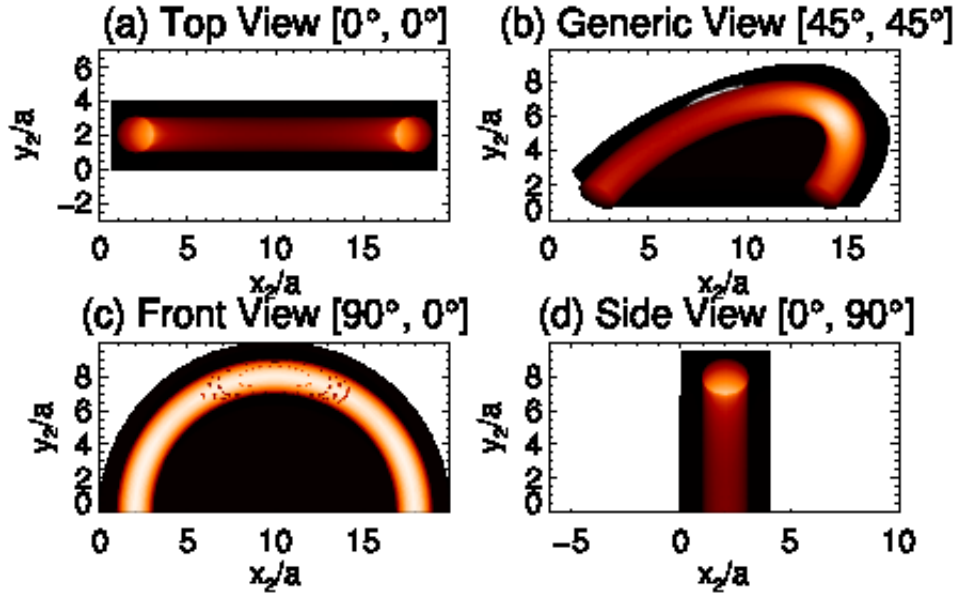


Fig. 3.— Fe IX $\lambda 171.073$ Å synthetic emission at (a) top view, (b) generic view, (c) front view and (d) side view. The origins and ranges of the plots are chosen to best match the relative geometries at various views, and will not affect the results at all. (This figure is also available as an mpeg animation in the electronic edition of the Astrophysical Journal)

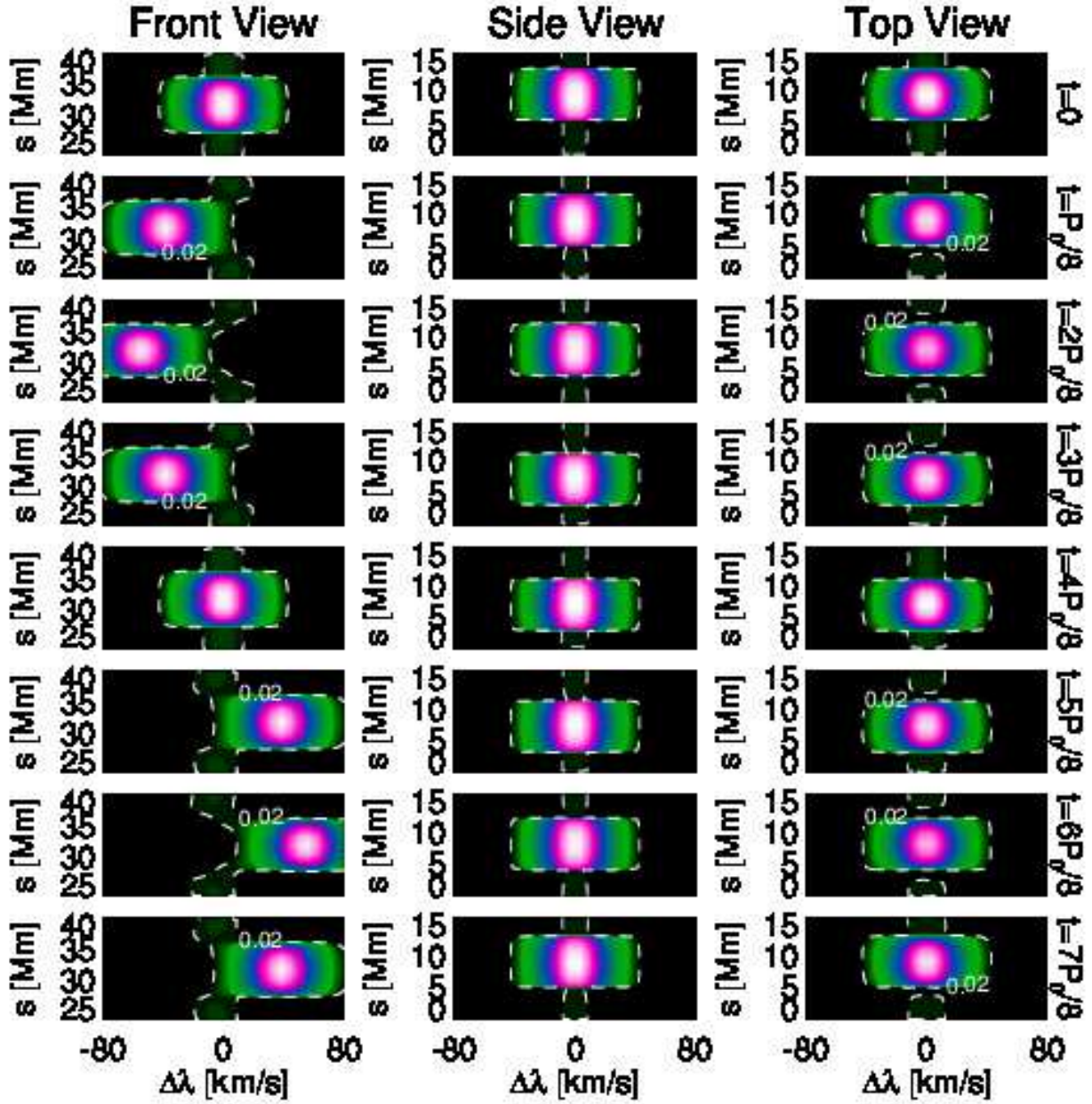


Fig. 4.— Fe IX $\lambda 171.073$ Å spectra of sit-and-stare modes along slices s across the loop apex at front view (left), side view (middle) and top view (right). The dashed lines contour the 0.02-level of the peak emission, and highlight the pendular motion at front view and rotational motion at top view. (This figure is also available as an mpeg animation in the electronic edition of the Astrophysical Journal)

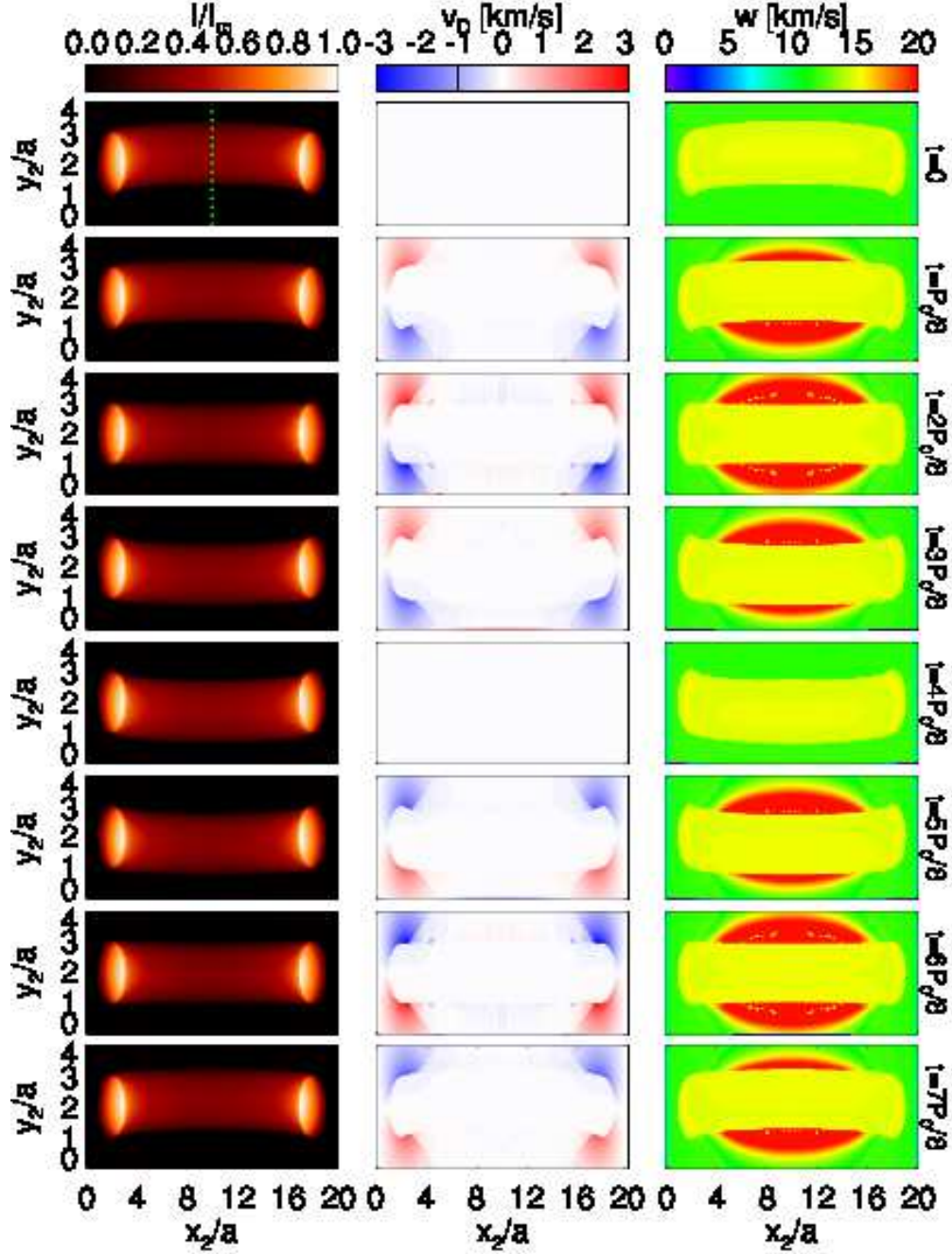


Fig. 5.— Snapshots of the relative emission I/I_m (left), Doppler shift velocity v_D (middle) and line width w (right). (This figure is also available as an mpeg animation in the electronic edition of the Astrophysical Journal)

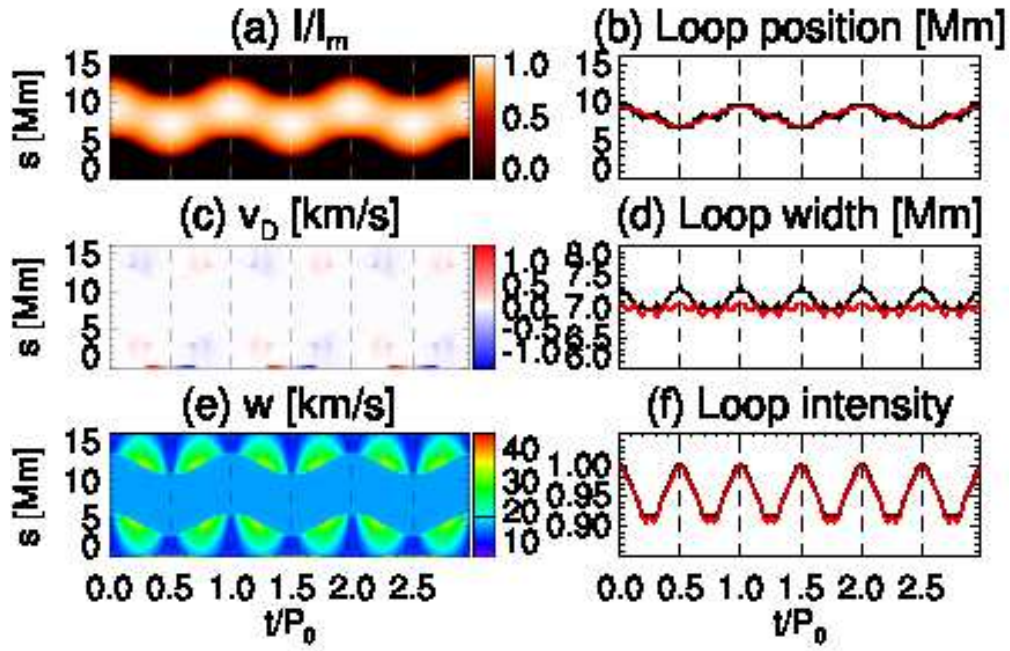


Fig. 6.— Sit-and-stare mode across the loop apex at top view in the Fe IX $\lambda 171.073$ Å line and the measurements of loop position, width and intensity. The red continuous lines plot the corresponding case in the EIS resolution.

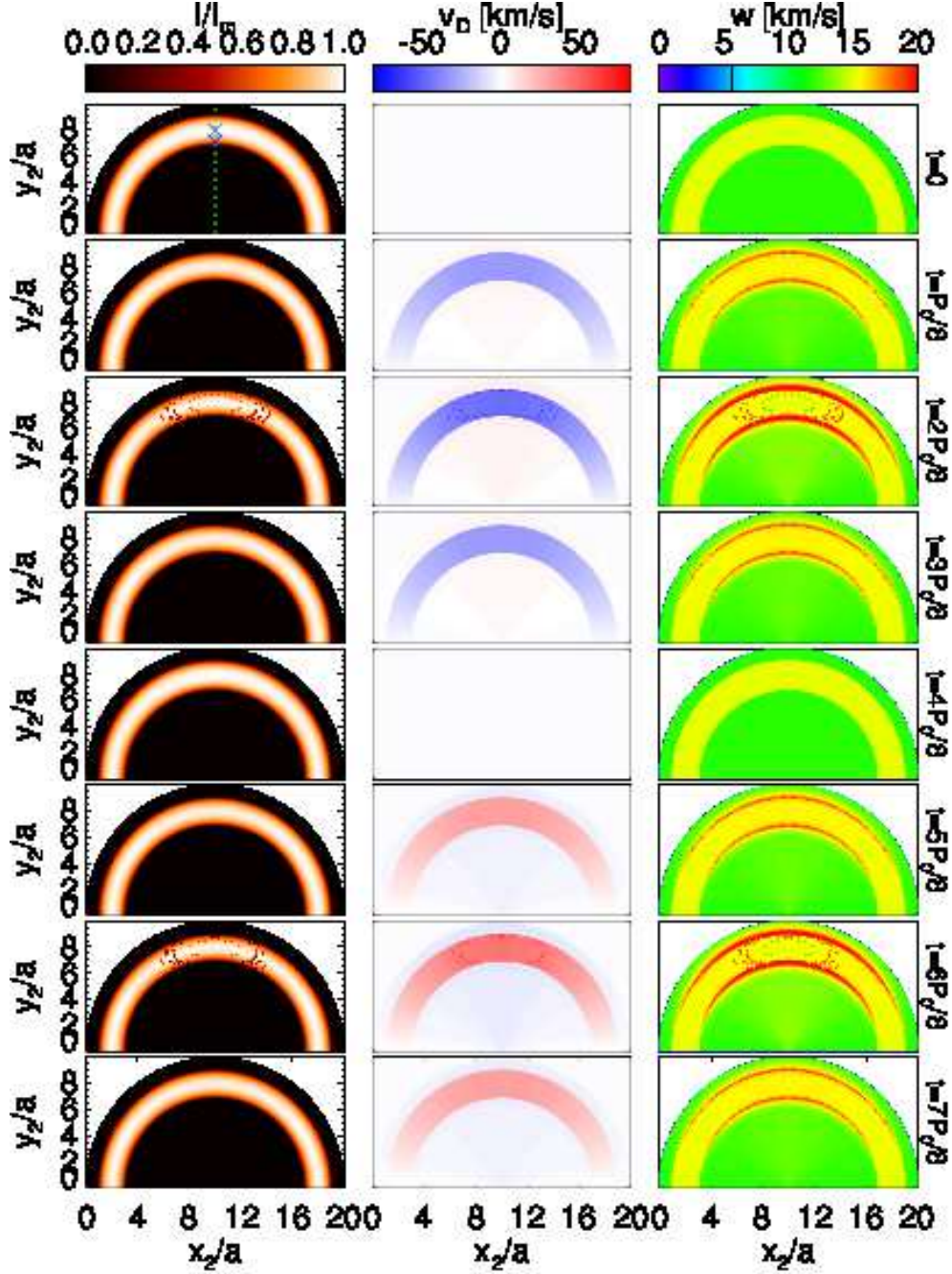


Fig. 7.— The same as Figure 5 but at front view. Two crosses mark the positions at $r = 0$ and $r = 0.8a$ and the associated dynamic spectra are illustrated in Figure 13. (This figure is also available as an mpeg animation in the electronic edition of the Astrophysical Journal)

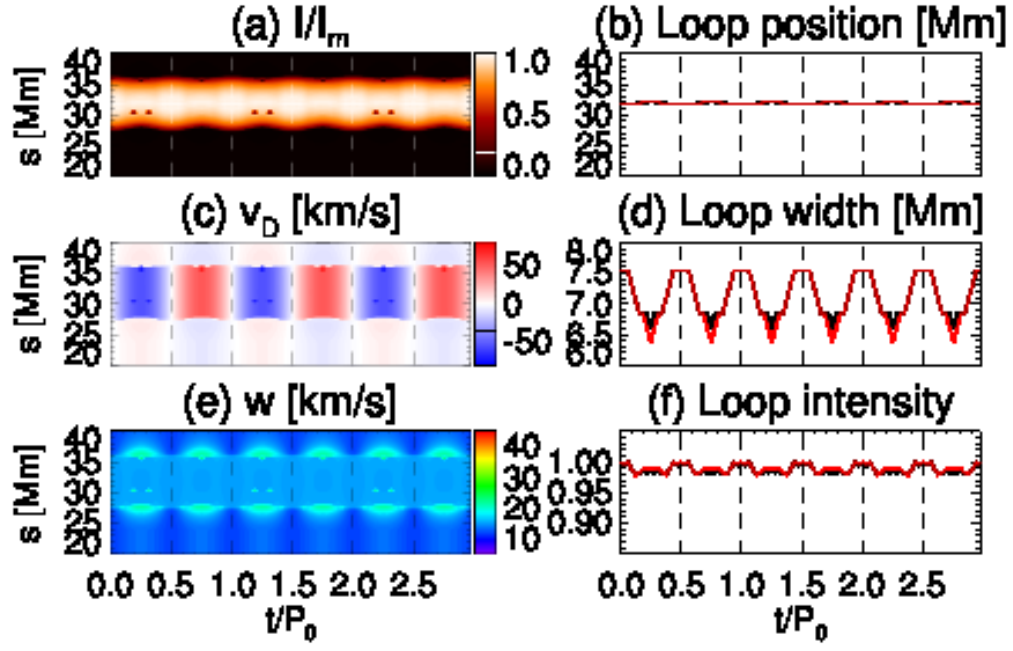


Fig. 8.— The same as Figure 6 but at front view.

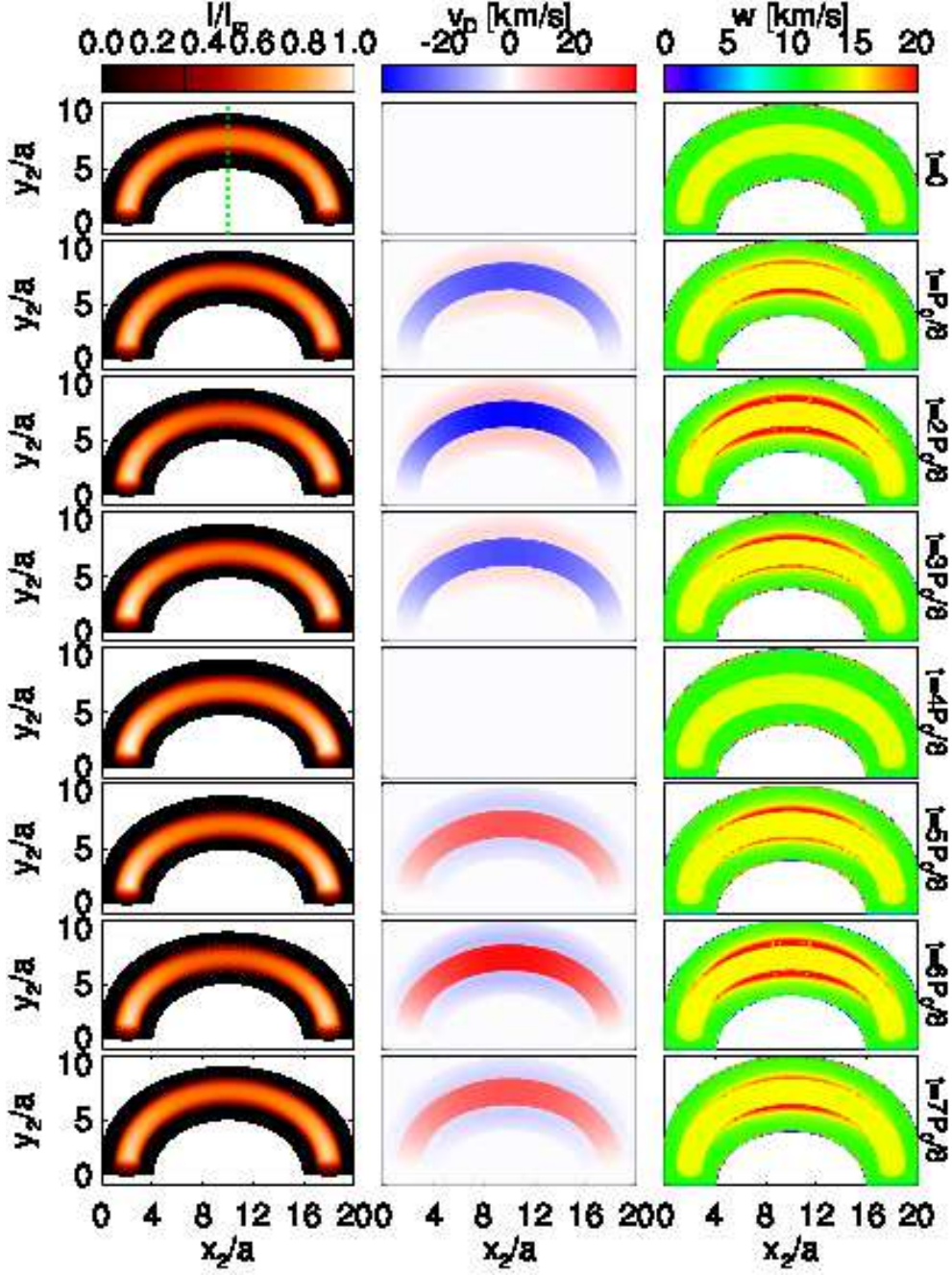


Fig. 9.— The same as Figure 5 but at oblique view. (This figure is also available as an mpeg animation in the electronic edition of the Astrophysical Journal)

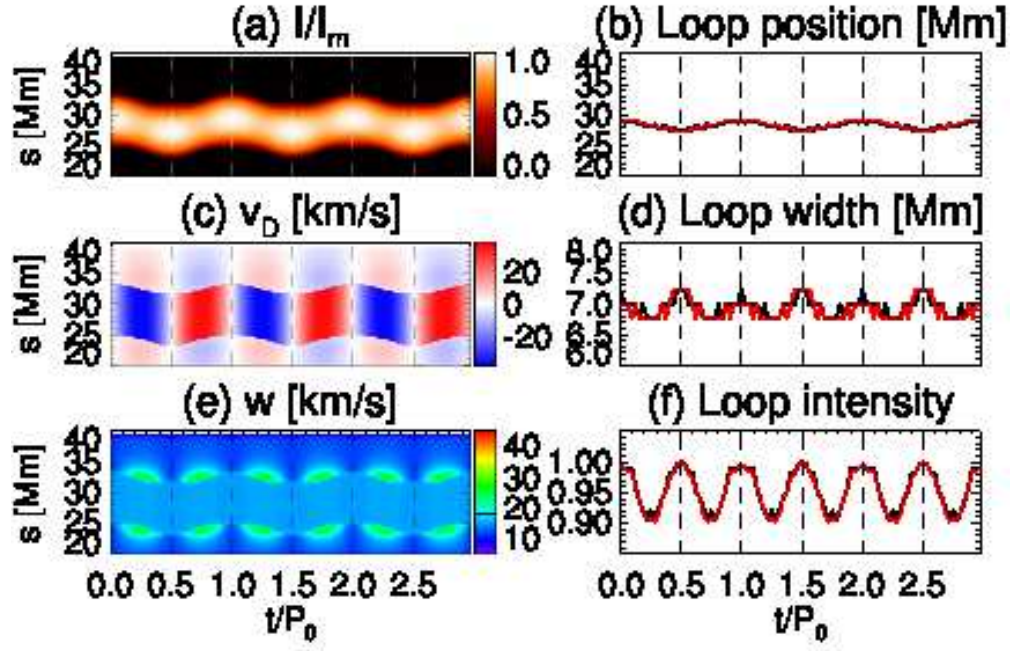


Fig. 10.— The same as Figure 6 but at oblique view.

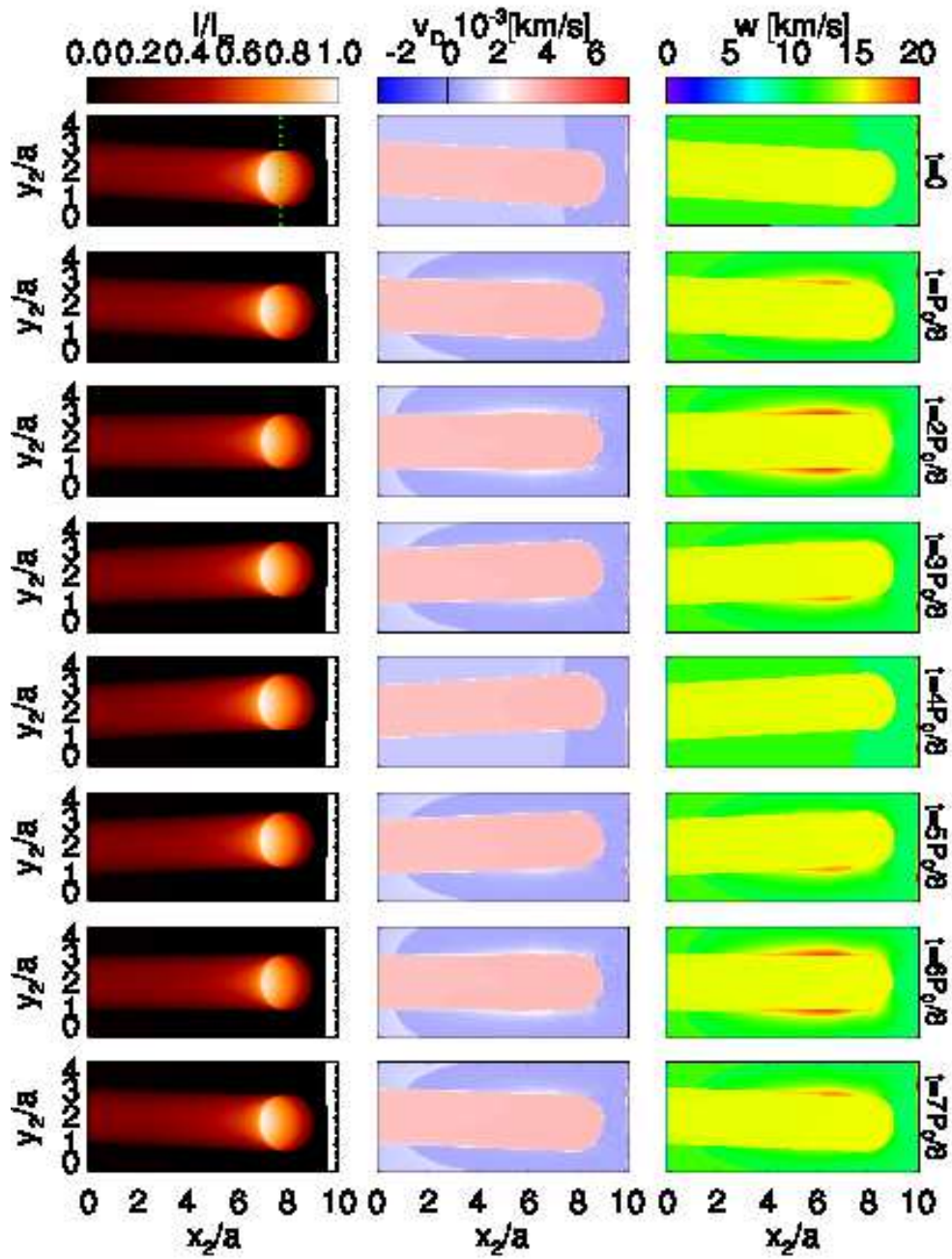


Fig. 11.— The same as Figure 5 but at side view. (This figure is also available as an mpeg animation in the electronic edition of the Astrophysical Journal)

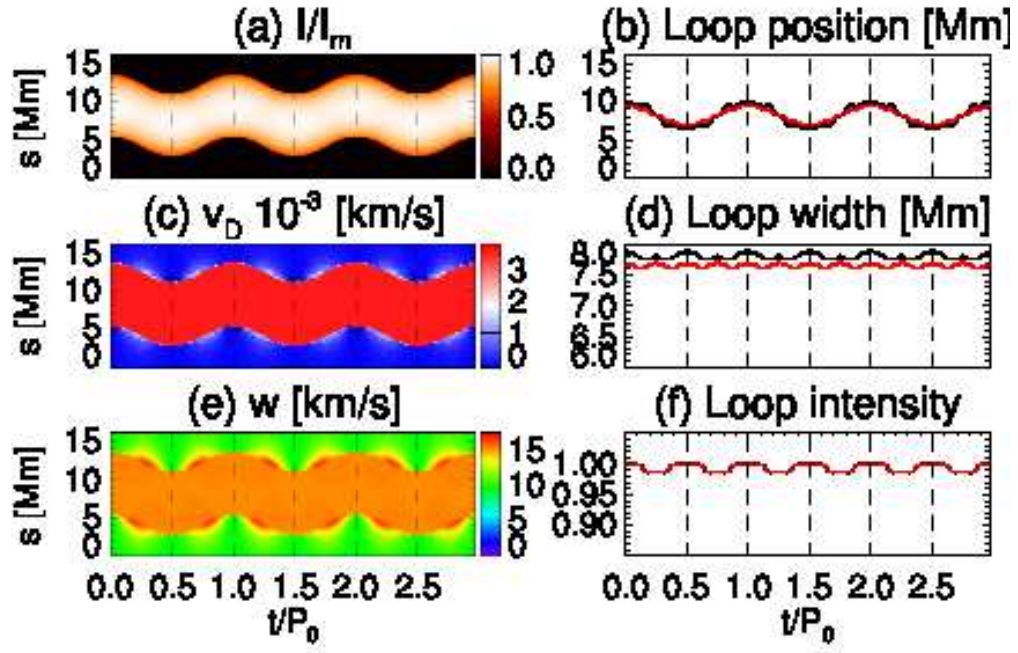


Fig. 12.— The same as Figure 6 but at side view.

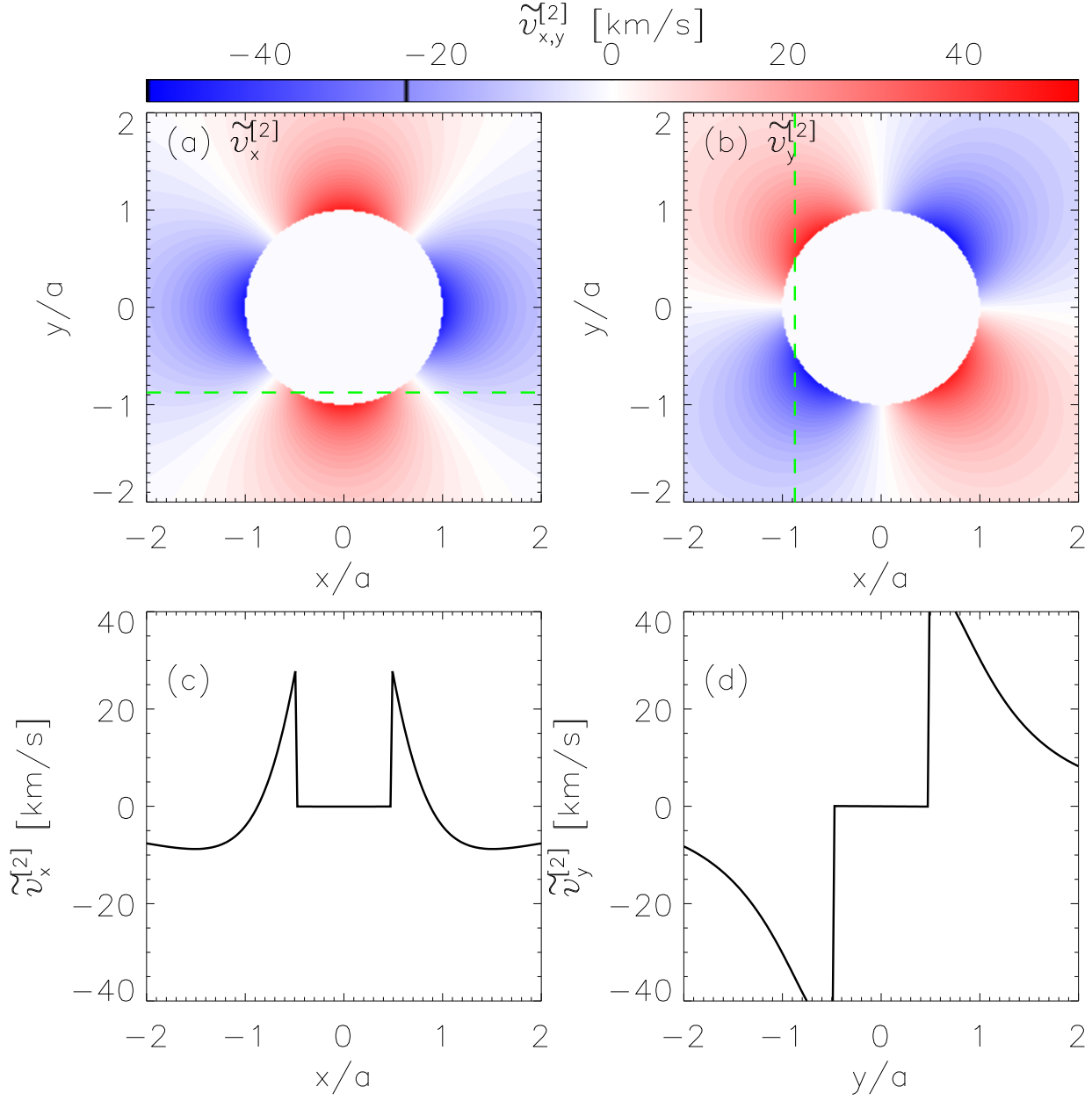


Fig. 14.— (a) and (b) Cross-sectional distribution of the quadrupole terms $\tilde{v}_x^{[2]}$ and $\tilde{v}_y^{[2]}$. (c) Profiles of $\tilde{v}_x^{[2]}$ along the horizontal dashed line marked in (a). (d) Profiles of $\tilde{v}_y^{[2]}$ along the vertical dashed line labeled in (b).

A. Derivation of the quadrupole terms

Here we demonstrate the derivation of Equation 27 and 29.

$$\tilde{v}_x = \hat{v}_r \cos^2 \phi - \hat{v}_\phi \sin^2 \phi, \quad (\text{A1})$$

$$= \frac{-A\omega\kappa_r}{\rho_0(\omega^2 - \omega_A^2)} \left(\frac{d\mathcal{R}}{\kappa_r dr} \cos^2 \phi + \frac{\mathcal{R}}{\kappa_r r} \sin^2 \phi \right). \quad (\text{A2})$$

We define $\lambda = \kappa_r r$ and $\mathcal{R}'(\lambda) = d\mathcal{R}/d\lambda$. For the plasma motion inside the loop $r < a$:

$$\frac{d\mathcal{R}}{\kappa_r dr} \cos^2 \phi + \frac{\mathcal{R}}{\kappa_r r} \sin^2 \phi = J_1'(\lambda) \cos^2 \phi + \frac{J_1(\lambda)}{\lambda} \sin^2 \phi \quad (\text{A3})$$

$$= \left(\frac{J_1}{\lambda} - J_2 \right) \cos^2 \phi + \frac{J_1(\lambda)}{\lambda} \sin^2 \phi \quad (\text{A4})$$

$$= \frac{J_1}{\lambda} - J_2 \cos^2 \phi \quad (\text{A5})$$

$$= \frac{J_1}{\lambda} - \frac{J_2}{2} - \frac{J_2}{2} \cos 2\phi \quad (\text{A6})$$

$$= \frac{J_0 - J_2 \cos 2\phi}{2}, \quad (\text{A7})$$

where we used $J_1'(\lambda) = J_1/\lambda - J_2$ and $J_2 = 2J_1/\lambda - J_0$ (Olver et al. 2010) in the derivation. We follow the same procedure and used $K_1' = K_1/\lambda - K_2$ and $K_2 = 2K_1/\lambda + K_0$ (Olver et al. 2010). Then we obtained the plasma motion outside the loop $r > a$:

$$\frac{d\mathcal{R}}{\kappa_r dr} \cos^2 \phi + \frac{\mathcal{R}}{\kappa_r r} \sin^2 \phi = K_1'(\lambda) \cos^2 \phi + \frac{K_1(\lambda)}{\lambda} \sin^2 \phi \quad (\text{A8})$$

$$= \frac{K_1}{\lambda} - K_2 \cos^2 \phi \quad (\text{A9})$$

$$= -\frac{K_0 + K_2 \cos 2\phi}{2} \quad (\text{A10})$$

Here, we obtain the horizontal motion,

$$\tilde{v}_x = \begin{cases} \frac{-A_i\omega|\kappa_{ri}|}{2\rho_i(\omega^2 - \omega_{Ai}^2)} (J_0 - J_2 \cos 2\phi), & \text{for } r \leq a \\ \frac{-A_e\omega\kappa_{re}}{2\rho_e(\omega^2 - \omega_{Ae}^2)} (-K_0 - K_2 \cos 2\phi), & \text{for } r > a. \end{cases} \quad (\text{A11})$$

$$(\text{A12})$$

At $r = 0$, $\tilde{v}_x = v_{00} = \frac{-A_i\omega|\kappa_{ri}|}{2\rho_i(\omega^2 - \omega_{Ai}^2)}$; while at $r = a$ and $\phi = 0$ or π ,

$$\tilde{v}_x|_{r=a^-} = v_{00}(J_0(|\kappa_{ri}|a) - J_2(|\kappa_{ri}|a)), \quad (\text{A13})$$

$$\tilde{v}_x|_{r=a^+} = \frac{-A_e\omega\kappa_{re}}{2\rho_e(\omega^2 - \omega_{Ae}^2)} (-K_0(\kappa_{re}a) - K_2(\kappa_{re}a)), \quad (\text{A14})$$

$$= \frac{J_1'(|\kappa_{ri}|a)}{K_1'(\kappa_{re}a)} v_{00} (-K_0(\kappa_{re}a) - K_2(\kappa_{re}a)). \quad (\text{A15})$$

where we recalled the total pressure balance at $r = a$ and the dispersion relationship (Equation 13):

$$A_i J_1(|\kappa_{ri}|a) = A_e K_1(\kappa_{re}a) \quad (\text{A16})$$

$$\frac{\rho_i(\omega_{Ai}^2 - \omega^2)\kappa_{re}}{\rho_e(\omega_{Ae}^2 - \omega^2)|\kappa_{ri}|} = \frac{J_1'(|\kappa_{ri}|a)K_1(\kappa_{re}a)}{J_1(|\kappa_{ri}|a)K_1'(\kappa_{re}a)}. \quad (\text{A17})$$

If we use the relationship $J'_1 = 0.5(J_0 - J_2)$ and $K'_1 = -0.5(K_0 + K_2)$ (Olver et al. 2010), then we could verify that $\tilde{v}_x|_{r=a^-} = \tilde{v}_x|_{r=a^+}$ at $\phi = 0$ and π .

If one follows the same procedure and uses the relationships ($J'_1 = J_1/\eta - J_2$ and $K'_1 = K_1/\eta - K_2$, Olver et al. 2010), then one could easily obtain the vertical component:

$$\tilde{v}_y = \begin{cases} -v_{00}J_2 \sin 2\phi, & \text{for } r \leq a \\ -\frac{J'_1(|\kappa_{ri}|a)}{K'_1(\kappa_{re}a)}v_{00}K_2 \sin 2\phi, & \text{for } r > a. \end{cases} \quad (\text{A18})$$